

# Analysis of Strength and Modal Characteristics of a Full Tubular Pump Impeller Based on Fluid-Structure Interaction

Lijian Shi (✉ [shilijian@yzu.edu.cn](mailto:shilijian@yzu.edu.cn))

Yangzhou University

**Jun Zhu**

Yangzhou University

**Li Wang**

Huai'an Institute of Hydraulic Survey and Design

**Shiji Chu**

International Center on small Hydro Power

**FangPing Tang**

Yangzhou University

**Yuhang Jiang**

Yangzhou University

**Tian Xu**

Yangzhou University

**Jie Yu**

Yangzhou University

---

## Research Article

**Keywords:** full tubular pump, axial-flow pump, deformation, stress, modal analysis, fluid-structure interaction, numerical simulation

**Posted Date:** June 24th, 2021

**DOI:** <https://doi.org/10.21203/rs.3.rs-627588/v1>

**License:** © ⓘ This work is licensed under a Creative Commons Attribution 4.0 International License.

[Read Full License](#)

---

# Analysis of Strength and Modal Characteristics of a Full Tubular Pump Impeller Based on Fluid-Structure Interaction

LiJian Shi<sup>a</sup>, Jun Zhu<sup>a</sup>, Li Wang<sup>b</sup>, ShiJi, Chu<sup>c</sup>, FangPing Tang<sup>a</sup>, YuHang Jiang<sup>a</sup>, Tian Xu<sup>a</sup>, Jie Yu<sup>a</sup>

a. College of Hydraulic Science and Engineering, Yangzhou University, 225000 Yangzhou, Jiangsu, China;

b. Huai'an Institute of Hydraulic Survey and Design Ltd, 223001 Huai an, Jiangsu, China

c. International Center on small Hydro Power, Hangzhou, 310002 Zhejiang, China;

Correspondence: (LiJian Shi) shilijian@yzu.edu.cn

**Abstract:** FSI(Fluid-Structure Interaction) is used to perform the the structural mechanical characteristics on the full tubular and the axial-flow pumps. The results show that as the flow rate increases, the total deformation and equivalent stress are significantly reduced. The MTD(max total deformation) and the MES(max equivalent stress) of the full tubular pump impeller appear at the outer edge of the blade. There are two stress concentrations in the full tubular pump impeller, in which one is located in the outlet area of the rim, and the other is located in the outlet area of the hub. However, the MES of the axial-flow pump appears at the center of the blade hub. The performance difference between the full tubular pump and the axial-flow pump is mainly caused by the clearance backflow. The natural frequency of the full tubular pump is lower than that of the axial-flow pump according to the modal results. The MES of the full tubular pump is mainly concentrated at the junction of the blade and the motor rotor, and the max thickness of the rim is 6mm, which is more prone to cracks, seriously affecting the safety and stability of the pump.

**Keywords:** full tubular pump; axial-flow pump; deformation; stress; modal analysis; fluid-structure interaction; numerical simulation.

---

## 1 Introduction

The full tubular pump is a new type of mechatronics product [1], which blades are connected with the motor rotor. Compared with the axial-flow pump, the full tubular pump eliminates the transmission equipment, and its structural advantage is very obvious. However, the efficiency of the full tubular pump impeller is generally lower than that of the axial-flow pump. Shi LJ et al. [2-4] used a combination of numerical simulation and model tests on the axial-flow and full tubular pumps. He concluded that the clearance backflow has a greater impact on the hydraulic performance of the full tubular pump by analyzing the characteristics of energy performance and pressure pulsation.

As the core component of the pump, the structural stress of the impeller is caused by periodic water pressure. Long-term operation will cause cracks or fatigue damage on the blade surface, which seriously threatens the safe and stable operation of the pump [5-8]. Therefore, the structural mechanical properties of impellers have attracted more and more attention, so the FSI analysis method has become an effective method to analyze the stress and deformation of the structure. Kan K et al. [9-10] applied the bidirectional FSI method to analyze the dynamic stress distribution of the blade. He found that the joint between the blade and the hub is the main stress concentration area and proposed measures to effectively relieve the stress concentration and detect the blade stress distribution. Schneider A et al. [11] studied the influence of impeller structure design parameters on the structural characteristics of multistage centrifugal pumps. Pei J et al. [12] quantitatively analyzed the blade deformation and stress distribution of the bidirectional axial-flow pump device under different flow conditions, and found that the maximum deformation and stress exist at the blade edge and the hub respectively. Zhang LJ et al. [13] discovered that the stress concentration at the blade hub is caused by the cantilever structure of the rotating blade. Li W et al. [14-15] conducted bidirectional FSI and modal analysis on the mixed-flow pump, and the results showed that fatigue failure was more likely to occur at the hub. At the same time, he also found that the natural frequency of vibration is not affected by the flow rate. Li CY et al. [16] explored that the vibration frequency of the bidirectional shaft extension pump device under zero head condition is very close to the first or second mode natural frequencies of the pump.

45 Deng ZP et al. [17] compared the unidirectional and bidirectional FSI of tidal turbines, and found that the predicted  
 46 power values of the two analysis methods are basically the same. The bidirectional FSI has a great advantage in  
 47 predicting the influence of tip vortices. Benra FK et al. [18] compared the unidirectional and bidirectional FSI solution  
 48 results of the single vane pump, and pointed out that the bidirectional FSI simulation result shown the good agreement  
 49 with the experiment. Zhu R et al. [19] found that the main distribution trend of wind turbine blade stress remains  
 50 unchanged whether the unidirectional or bidirectional FSI method is adopted. In view of the unidirectional or  
 51 bidirectional FSI prediction results, Javanmardi N et al. [20] found that both methods can better predict the  
 52 hydrodynamic characteristics of the propeller. Wijesooriya K et al. [21] proposed a non-coupled unidirectional FSI  
 53 analysis method for super-tall structures, and verified its feasibility and calculation accuracy.

54 The above research conclusions found that the MES of the impeller is mainly concentrated at the hub of the blade.  
 55 However, for a special type of pump such as a full tubular pump, the research conclusions on the stress and deformation  
 56 of the structure are not yet known. Hence, this paper adopts the unidirectional FSI method to compare the hydraulic and  
 57 structural mechanical characteristics of axial-flow and full tubular pump impellers under different flow conditions. The  
 58 purpose of this research is to explore the structural characteristics of the full tubular pump and provide certain guidance  
 59 for the structural design of the full tubular pump.

## 60 2. Calculation method

61 The internal flow of the pump is a three-dimensional incompressible flow, and the control equation adopts the RANS  
 62 Reynolds average equation. Therefore, this simulation uses the finite volume method to discretize the control equations  
 63 and introduces the standard  $k$ - $\varepsilon$  turbulence model to simulate the three-dimensional turbulent flow. The standard  $k$ - $\varepsilon$   
 64 turbulence mode revises the turbulent viscosity considering the rotation and rotation flow conditions in the average flow,  
 65 and can better handle flows with high strain rates and large streamline curvatures. In the standard  $k$ - $\varepsilon$  turbulence model,  $k$   
 66 and  $\varepsilon$  are two basic unknowns. The corresponding transportation equations are shown as follows[22].

$$\frac{\partial(\rho k)}{\partial t} + \frac{\partial(\rho k u_i)}{\partial x_i} = \frac{\partial}{\partial x_j} \left[ \left( \mu + \frac{\mu_t}{\sigma_k} \right) \frac{\partial k}{\partial x_j} \right] + G_k + G_b - \rho \varepsilon - Y_M + S_k, \quad (1)$$

$$\frac{\partial(\rho \varepsilon)}{\partial t} + \frac{\partial(\rho \varepsilon u_i)}{\partial x_i} = \frac{\partial}{\partial x_j} \left[ \left( \mu + \frac{\mu_t}{\sigma_k} \right) \frac{\partial \varepsilon}{\partial x_j} \right] + C_{1\varepsilon} \frac{\varepsilon}{k} (G_k + C_{3\varepsilon} G_b) - C_{2\varepsilon} \rho \frac{\varepsilon^2}{k} + S_\varepsilon, \quad (2)$$

$$\mu_t = \rho C_\mu \frac{k^2}{\varepsilon},$$

$$G_k = \mu_t \left( \frac{\partial u_i}{\partial x_j} + \frac{\partial u_j}{\partial x_i} \right) \frac{\partial u_i}{\partial x_j}, G_b = 0, Y_M = 0, S_k = 0, S_\varepsilon = 0 \quad (3)$$

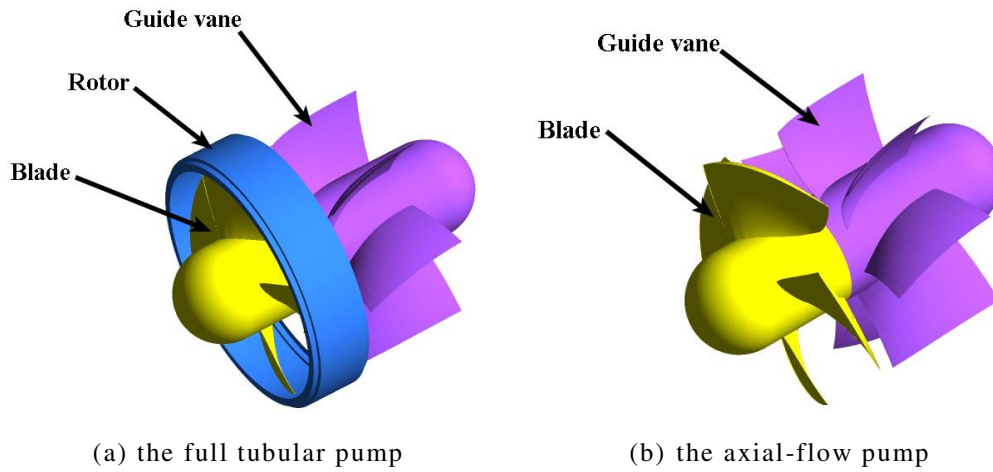
$$C_{1\varepsilon} = 1.44, C_{2\varepsilon} = 1.92, C_\mu = 0.09, \sigma_k = 1.0, \sigma_\varepsilon = 1.3$$

67 where  $\mu_t$  is the turbulence viscosity,  $C_\mu$  is constant,  $G_k$  is the generation term of turbulent kinetic energy  $k$  caused by average  
 68 velocity gradient,  $G_b$  is the generation term of turbulent kinetic energy  $k$  caused by buoyancy,  $Y_M$  is the contribution of  
 69 pulsation expansion in compressible turbulent pulsation,  $C_{1\varepsilon}$ ,  $C_{2\varepsilon}$  and  $C_{3\varepsilon}$  are empirical constants,  $\sigma_k$  and  $\sigma_\varepsilon$  are the Prandtl  
 70 Numbers corresponding to turbulent kinetic energy  $k$  and dissipation rate  $\varepsilon$  respectively,  $S_k$  and  $S_\varepsilon$  are user-defined source  
 71 terms.  
 72

### 73 2.1 Object

74 The full tubular pump device studied in this paper is composed of the inlet pipe, the impeller, the rotor, the guide vane

75 and the outlet pipe, as shown in Fig.1(a). The axial-flow pump does not contain the motor rotor, the rest of the hydraulic  
 76 components are consistent with the full tubular pump, as shown in Fig.1(b). The main design parameters of the pump  
 77 model are shown in Table.1 below.



80 Figure. 1 The pump model type

81 Table. 1 The main design parameters of the pump device

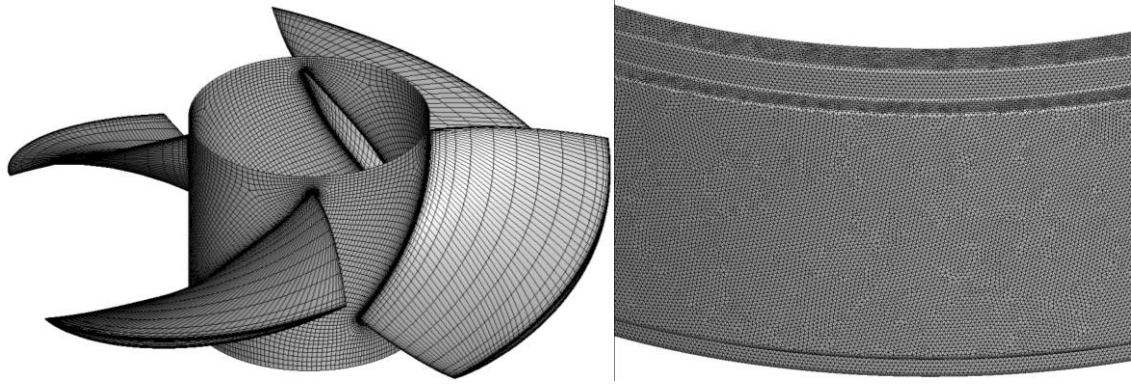
Parameter	Impeller diameter	Rotation speed	Design flow	Design head	Blade number	Guide vane number
	$D(\text{mm})$	$n(\text{r/min})$	$Q_{bep}(\text{L/s})$	$H(\text{m})$		
Value	350	950	390	3.2	4	7

82 *2.2 Boundary conditions*

83 Multiple reference coordinate systems are used to calculate the fluid domain. The impeller which is a rotating  
 84 component adopts a rotating coordinate system, and the rest of the components which are static domain adopt a  
 85 stationary coordinate system. In the steady-state calculation, the "Stage" model is used to process the data transfer of the  
 86 interface between the rotating domain and the stationary domain. The interface characteristic is to ignore the  
 87 nonuniformity of the flow in the circumferential direction. The solid wall of the computational fluid domain is set to the  
 88 no slip wall, and the standard wall function is used to predict the flow of the wall boundary layer in the near-wall area.  
 89 The inlet boundary condition is set to total pressure which value is 1 atm. The outlet boundary condition is set to mass  
 90 flow rate.

91 *2.3 Grid*

92 The computational domains of the whole flow passage are dispersed as structured grids except for the motor rotor  
 93 applies unstructured grids. The components are divided into grids and assembled in CFX to obtain the entire device  
 94 calculation domain. The grid is taken for the main carrier of numerical simulation calculation, in which the quality and  
 95 quantity directly affect the accuracy of computational results. The impeller is the rotating part of the entire computational  
 96 domain, and the number of its grids has a greater influence on the computational accuracy. According to reference [4],  
 97 when the single passage impeller grid reaches 140,000, the number of grids has little effect on the computational results.  
 98 Therefore, the final single passage impeller grid number reaches 140,000 approximately. As the same time, the first  
 99 dimensionless  $y^+$  value of the blade wall boundary layer fluctuate around 30, which meets the use conditions of the  
 100 turbulence model. The Fig. 2 presents the generated grid of the impeller and motor rotor.



(a) blade (b) rotor

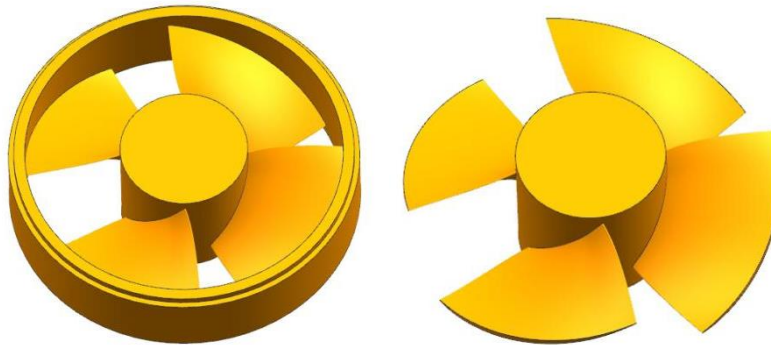
Figure.2 The generated grid of the impeller and rotor

#### 2.4 FSI setting

The structural analysis in this paper adopts the unidirectional FSI method, and the structural calculation uses the finite element method to analyze the structural characteristics of the blade. The structural model only takes into account the impeller, as shown in Figure 3. The material properties of the impeller are stainless steel, and the characteristic parameters of the stainless steel are shown in Table 2. Fig. 4 shows the structural grid of the impeller. The impeller structure is divided into tetrahedral grids, in which the full tubular pump impeller grid number is 941,001 and the axial-flow pump impeller grid number is 728,706. The dynamic equation for structural calculations is defined as follows [23].

$$[M](\ddot{x}) + [C](\dot{x}) + [K](x) = \{F\}, \quad (3)$$

where [M] is the structural mass matrix, [C] is the structural damping matrix, [K] is the structural stiffness matrix, (x) is the structural displacement, ( $\dot{x}$ ) is the structural velocity, ( $\ddot{x}$ ) is the structural acceleration, and {F} represents the flow field force of the structure under the FSI.

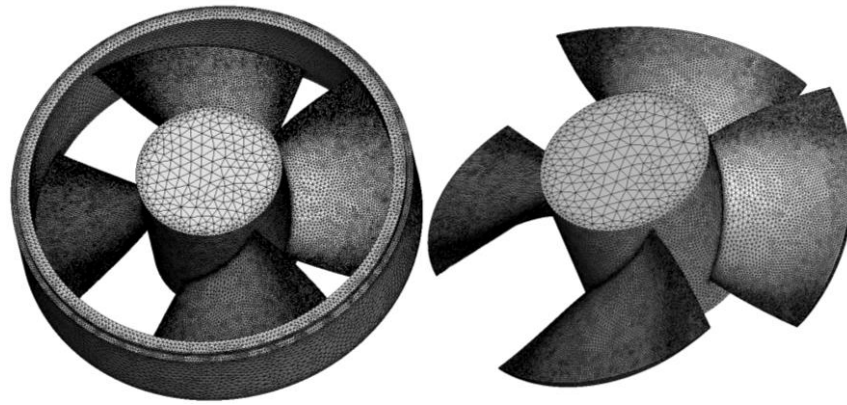


(a) the full tubular pump impeller (b) the axial-flow pump impeller

Figure. 3 Impeller structure model

Table. 2 The material properties of the impeller

Patameter	Density $\rho/(\text{kg}\cdot\text{m}^{-3})$	Young modulus $E/\text{MPa}$	Poisson ratio $\mu$	Yield strength $\sigma_s/\text{MPa}$
Value	7780	203	0.29	550

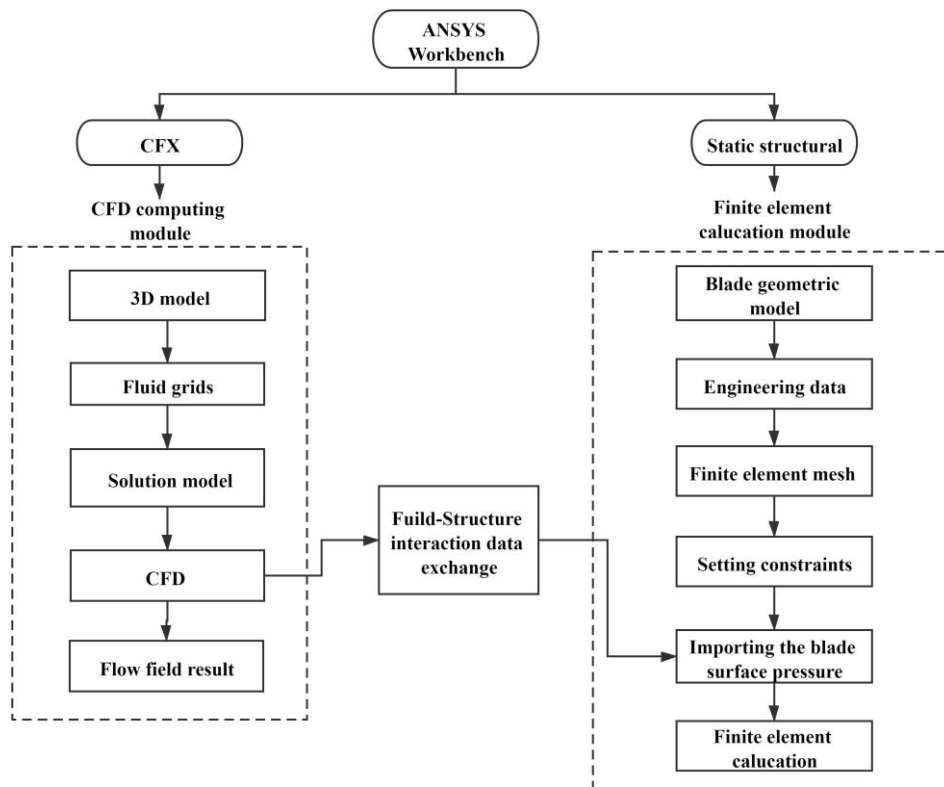


(a) the full tubular pump impeller grid (b) the axial-flow pump impeller grid.

Figure.4 The structural grid of the impeller

120  
121  
122  
123  
124  
125  
126  
127  
128

Finite element calculations need to consider the boundary conditions of the blade model, mainly including structural constraints and loads. In order to prevent the structure from generating rigid body displacement, a fixed constraint is adopted on the hub surface. The load conditions for the structure calculation are transmitted through the surface pressures of the blade, hub, rim, and rotor calculated by CFD. In addition, taking into account the centrifugal force caused by the rotation of the impeller and the influence of gravity, the blade rotation speed ( $n$ ) is set to 950 r/min and the gravitational acceleration ( $g$ ) is set to  $9.81 \text{ m/s}^2$ . The FSI calculation process is shown in Fig.5.



129  
130  
131  
132  
133  
134  
135

Figure. 5 Flow chart of the FSI simulation

### 2.5 Model Experiment Verification

The model experiments include the axial-flow pump and the full tubular pump. The impeller diameter  $D$  is 350mm, the blade rotation speed  $n$  is 950 r/min, the hub ratio is 0.4, the number of blade is 4, the number of guide vane is 7. The pump test bench is shown in Fig. 6.

The pump device model experiment was carried out on the high-precision hydraulic machinery test bench , which was

136 a vertical closed circulation system. The energy performance test of the pump device is carried out in accordance with  
 137 SL140-2006 code requirement. The comprehensive error of the efficiency is  $\pm 0.39\%$ .

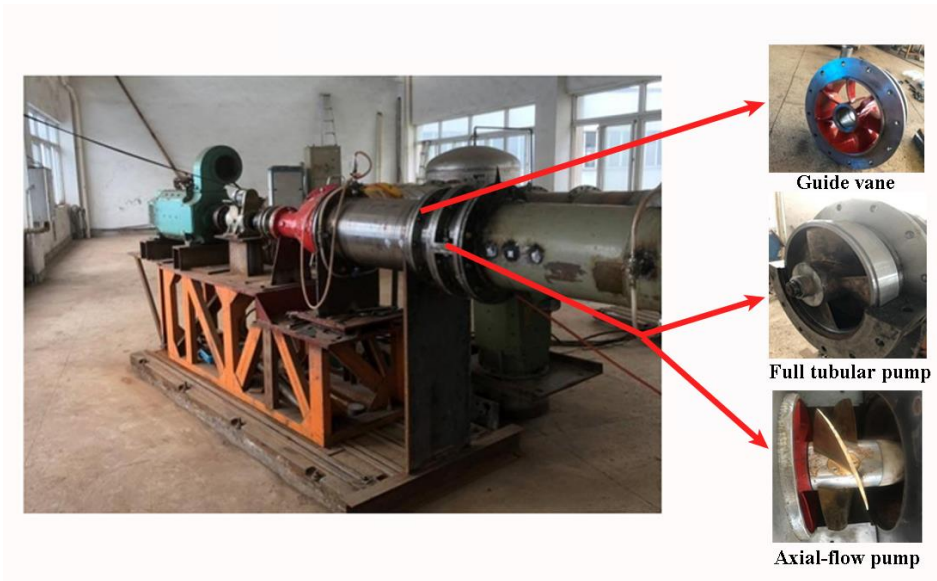


Figure. 6 The model test bench for the pump device

138  
 139  
 140 Fig. 7 shows the comparison between the numerical simulation and model test results of the axial-flow pump and the  
 141 full tubular pump. The variation trend of  $Q-H$  curve predicted by numerical simulation is basically consistent with that of  
 142 model experiment. The  $Q-H$  curve of the full tubular pump is significantly lower than that of the axial-flow pump. Under  
 143 the design condition  $Q_{bep}$ , the test operation head of the full tubular pump is 3.13 m, and the test operation head of the  
 144 axial-flow pump is 3.31 m. The head is increased by 5 % compared with that of the full tubular pump. The main reason  
 145 for this difference is caused by the clearance backflow [2-4]. Within the flow range of  $0.8Q_{bep}-1.2Q_{bep}$ , the relative error  
 146 between the experiment head and the predicted head of CFD is within 3%. Therefore, the numerical simulation results  
 147 have high credibility.

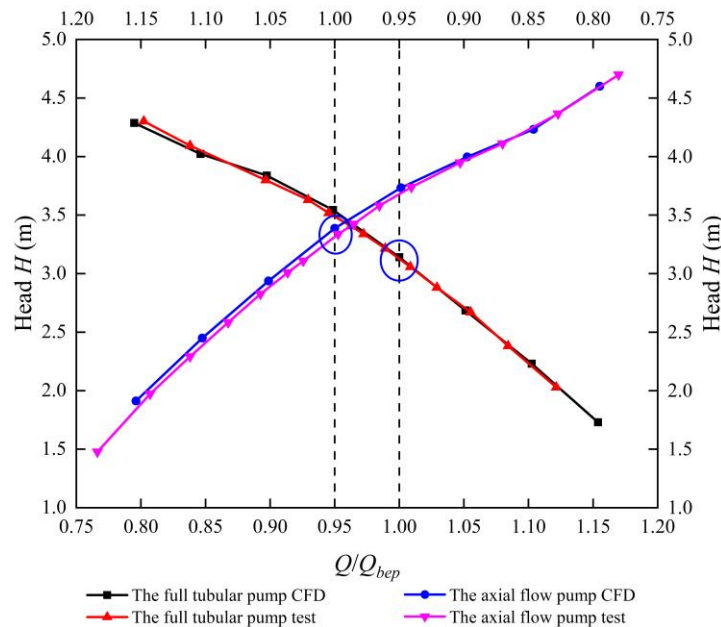


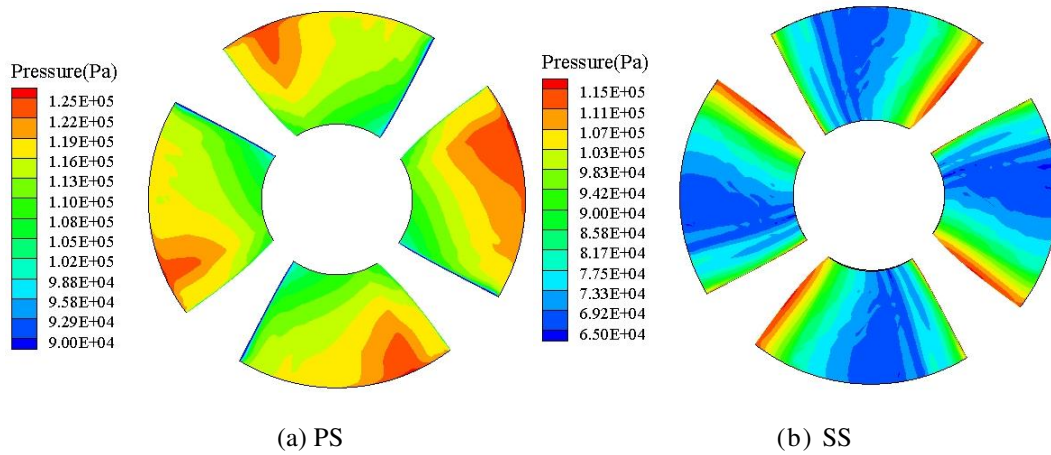
Figure. 7 Performance curve verification

148  
 149  
 150 **3 Results**

151 **3.1 Flow field analysis**

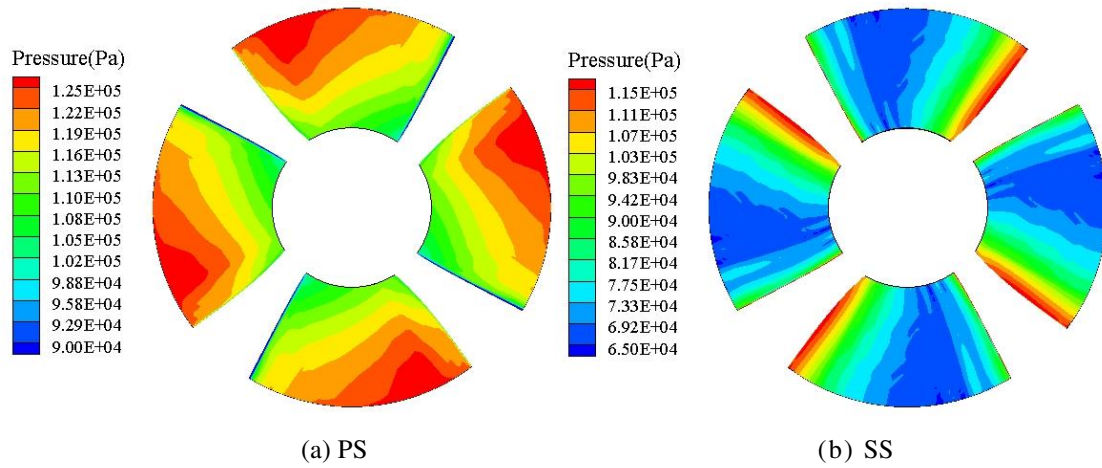
152 In the structural analysis, the pressure distribution on the blade surface is loaded on the structure as boundary condition

153 for finite element calculation. Therefore, the research on the surface pressure distribution establishes the foundation for  
154 the FSI analysis.



155  
156  
157

Figure. 8 Pressure distribution on the blade surface of the full tubular pump under the flow  $Q_{bep}$



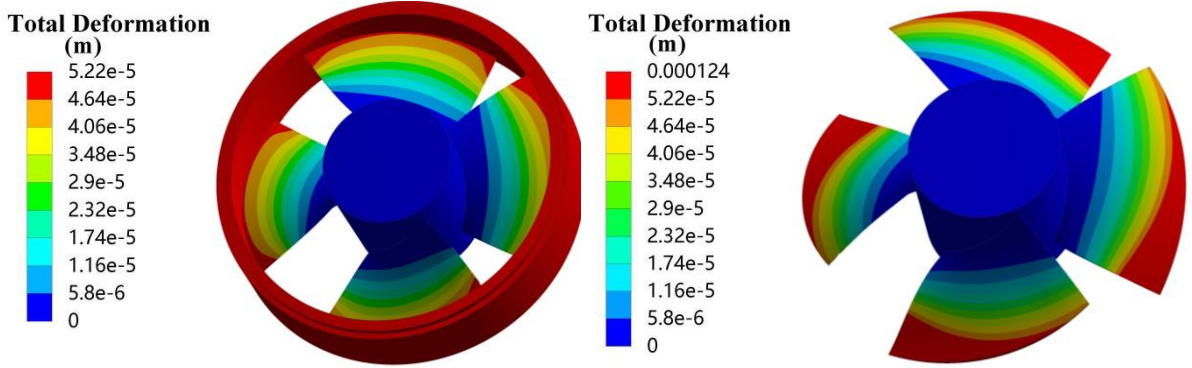
158  
159  
160

Figure. 9 Pressure distribution on the blade surface of the axial-flow pump under the flow  $Q_{bep}$

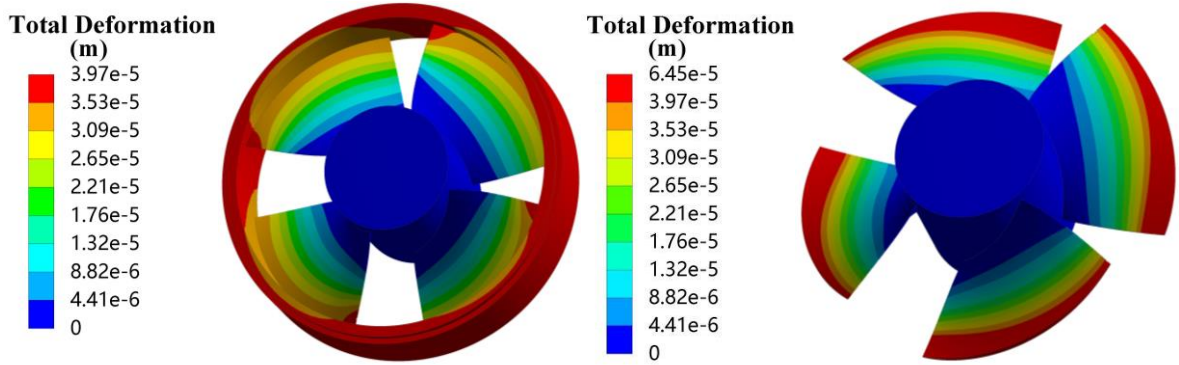
161 Fig. 8 and 9 are the cloud figure of pressure distribution on blade surface of the full tubular pump and axial-flow pump  
162 under the flow  $Q_{bep}$  respectively. The pressure distribution trends of blade surface of the full tubular pump and axial-flow  
163 pump are basically the same. The pressure of the blade PS (pressure surface) gradually increases from hub to rim, and the  
164 high pressure area is concentrated at the blade rim. The pressure of the blade SS (suction surface) decreases first and then  
165 increases from inlet to outlet, and the low pressure area is concentrated near the LE (leading edge) of the blade.

### 166 3.2 Structural deformation analysis

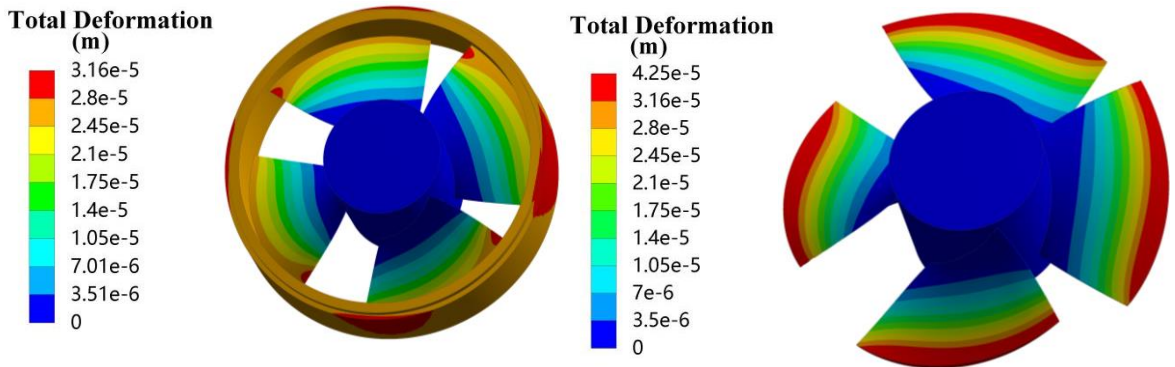
167 In order to accurately obtain the deformation and stress distribution of the full tubular pump and the axial-flow pump,  
168 the fluid calculation result needs to be transmitted to the corresponding position in the structure calculation. The pressure  
169 load of the full tubular pump includes the blades, hub, rim and rotor surface, and the axial-flow pump includes the blades  
170 and hub surface. According to the results of pressure transfer, 100 % of mechanical nodes in the structure analysis were  
171 mapped to the CFD surface.



(a) The total deformation under  $0.8Q_{bep}$



(b) The total deformation under  $Q_{bep}$



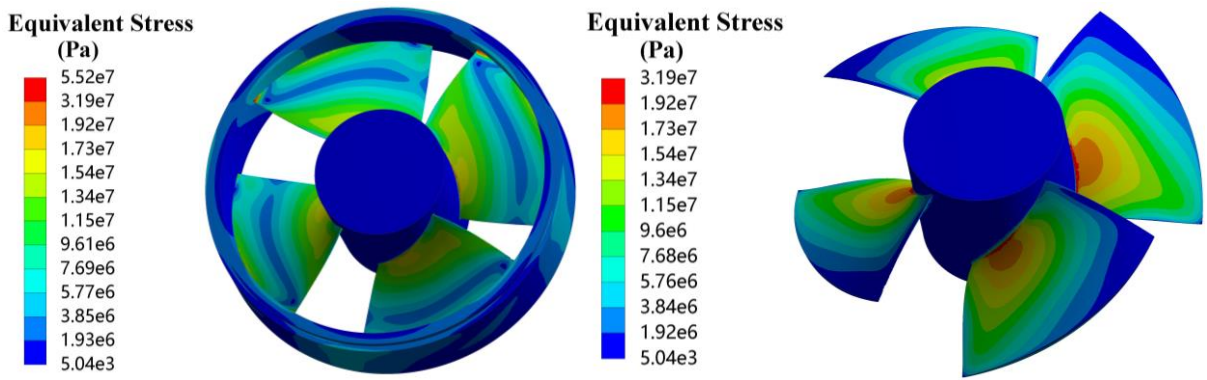
(c) The total deformation under  $1.1Q_{bep}$

Figure.10 Deformation distribution of full tubular pump and axial-flow pump

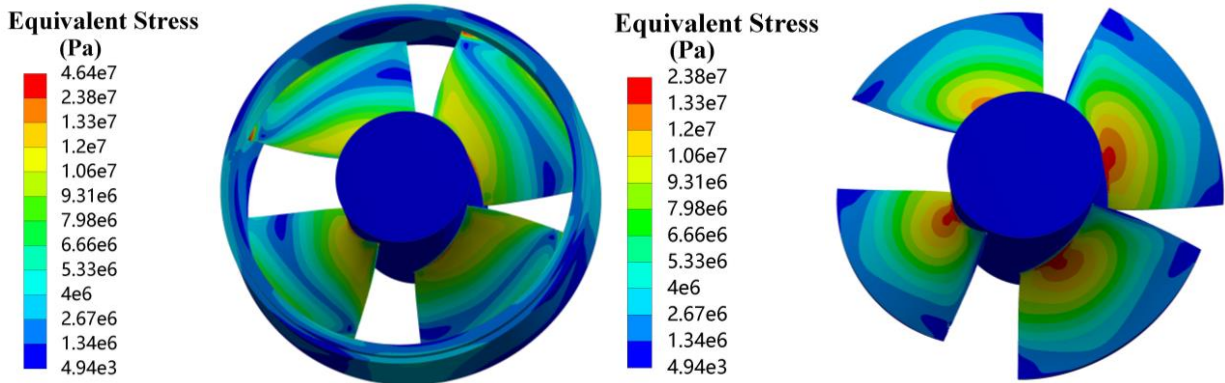
Fig. 10 demonstrates the total deformation of the full tubular pump and axial-flow pump under the flow conditions of  $0.8Q_{bep}$ ,  $Q_{bep}$  and  $1.1Q_{bep}$ , respectively. It can be seen that the blade deformation gradually increases from the hub to the rim, and the maximum deformation occurs at the blade rim. The maximum deformation of the axial-flow pump is mainly located at the inlet of the blade rim, while the maximum deformation of the full tubular pump is located at the outlet of the blade rim. As the flow rate increases, the pump head decreases, the axial force on the blade decreases, and the total deformation of the blade gradually decreases. When the flow condition  $Q=0.8Q_{bep}$ , the MTD of the full tubular pump is 0.052mm, and the MTD of the axial-flow pump is 0.12mm, which is 2.3 times that of the full tubular pump. When  $Q=1.0Q_{bep}$ , the MTD of the full tubular pump is 0.04mm, while the MTD of the axial-flow pump is 0.065mm, which is 1.63 times that of the full tubular pump. When  $Q=1.1Q_{bep}$ , the MTD of the full tubular pump is 0.032mm, while the MTD of the axial-flow pump is 0.043mm, which is 1.34 times that of the full tubular pump. The MTD of the full tubular pump under all flow conditions is smaller than that of the axial-flow pump. The MTD of the pump blade can be reduced when the blade of the full tubular pump is fixed with the rotor.

191 3.3 Structural stress analysis

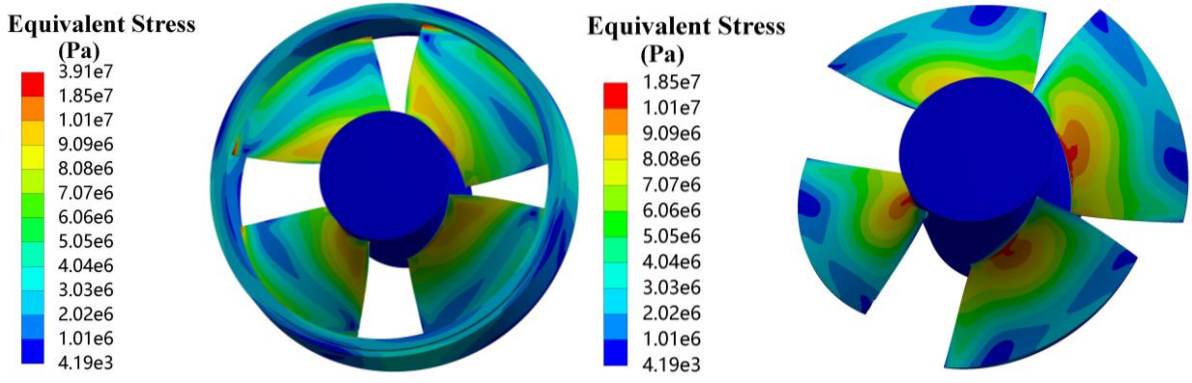
192 Fig. 11 reveals the difference in the equivalent stress distribution between the full tubular pump and the axial-flow pump. The equivalent stress of the full tubular pump decreases first and then increases from the hub to the rim. At the  
 193 same time, the MES appears at the rim of the impeller trailing edge, and there is also an obvious stress concentration area  
 194 on the outlet side of the hub. However, the equivalent stress of the axial-flow pump decreases from the hub to the rim,  
 195 and the equivalent stress is the smallest at the TE(trailing edge) of the rim. The MES of the axial-flow pump occurs in the  
 196 middle of the hub. The distribution trend of the equivalent stress under different flow conditions is basically the same,  
 197 and the MES value decreases with the increase of the flow condition. The MES of the full tubular pump is higher than  
 198 that of the axial-flow pump at the same flow condition. Under  $Q=0.8Q_{bep}$ , the MES of the full tubular pump reaches  
 199 55MPa, and that of the axial-flow pump reaches 31.9MPa. Under  $Q=Q_{bep}$ , the MES of the full tubular pump is 46.4MPa,  
 200 and that of the axial-flow pump is 23.8MPa. Under  $Q=1.1Q_{bep}$ , the MES of the full tubular pump is 39.1MPa, and that of  
 201 the axial-flow pump is 18.5MPa. However, the MES of the axial-flow pump and the full tubular pump is both lower than  
 202 the allowable stress of the material 190MPa.  
 203



204  
 205 (a) the equivalent stress under  $0.8Q_{bep}$



206  
 207 (b) the equivalent stress under  $Q_{bep}$



(c) the equivalent stress under  $1.1Q_{bep}$

Figure. 11 Equivalent Stress distribution of full tubular pump and axial-flow pump

208

209

210

211

212

213

214

215

216

217

218

219

220

221

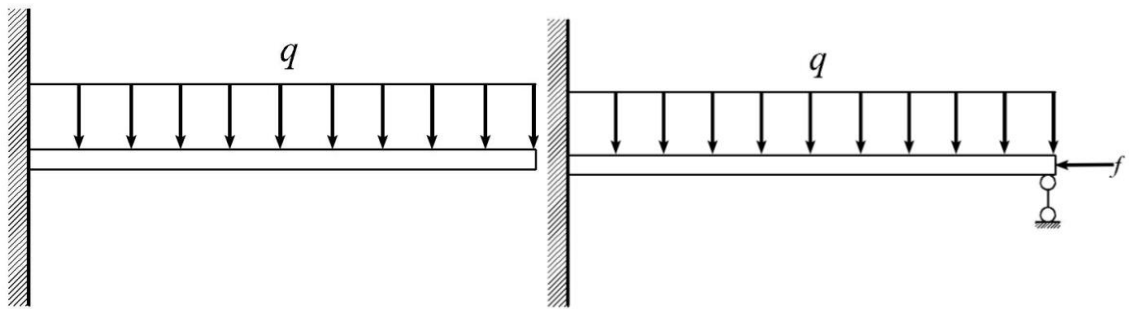
222

223

224

225

According to the distribution law of the total deformation and equivalent stress of the above-mentioned full tubular pump and axial-flow pump, the reasons for the difference in the distribution trend are analyzed. The axial-flow pump impeller can be simplified as a cantilever beam structure fixed at one end, and the pressure difference between the PS and SS acting on the blade can be regarded as the distributed load  $q$ , as shown in Fig. 12(a). Because the blade rim is the main part of the work, and the thickness of the blade is relatively thin. The maximum thickness of the rim airfoil is 6mm, and the maximum thickness of the hub airfoil is 12mm, which is likely to cause insufficient rigidity of the blade rim. As a result, the MTD occurs at the blade rim, and the MES occurs at the blade hub. The full tubular pump can be simplified to a structure with one end fixed and one end hinged, as shown in Fig. 12(b). Since both ends of the blade are constrained, the structural deformation can be restricted to a certain extent, and under the action of the lateral pressure  $f$ , the internal interaction force of the blade structure is enhanced. Because of the small structural deformation, the blade cannot release the stress through the deformation. Therefore, there are two stress concentrations, one of which is located in the outlet of the blade rim and the other is located in the outlet of the hub. The MES and MTD are located at the junction of the blade rim and the rotor, where the maximum thickness is relatively thin. The maximum thickness of the rim airfoil is 6 mm, which is most prone to fracture. In summary, the structure of the full tubular pump should attach great importance to the processing method at the junction of the blade rim and the rotor to avoid cracks because of the deformation and stress.



226

(a) the axial-flow pump

(b) the full tubular pump

Figure. 12 Simplified figures of impeller structural mechanics

227

228

229

230

231

232

From the above comparison, it is found that the equivalent stress at the blade rim of the full tubular pump has a large variation. Therefore, in order to analyze the distribution trend of the equivalent stress at this place in detail, a wire frame path is arranged around this place to summarize the equivalent stress distribution regularity from the PS to the SS. Fig. 13 shows the rim wire frame path of the full tubular pump.

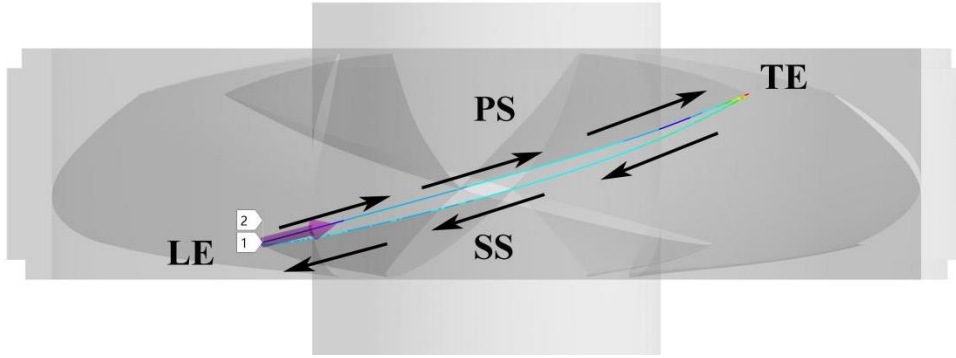


Figure. 13 The wire frame path at the blade rim

Fig. 14 presents the equivalent stress distribution trend at the blade rim under different flow conditions. The equivalent stress of the full tubular pump is obviously higher than that of the axial-flow pump. And it presents the distribution trend that the largest in the middle and the smallest on both sides. There are large stress fluctuations at the TE. However, the equivalent stress of the axial-flow pump presents a distribution trend that the smallest in the middle and the largest on both sides. Especially the stress at the rim outlet of the full tubular pump is significantly higher than that of the axial-flow pump. And the equivalent stress of the full tubular pump reaches 28.6MPa under  $Q=0.8Q_{bep}$ . The equivalent stress of the full tubular pump is 24.1MPa under  $Q=Q_{bep}$ . The equivalent stress of the full tubular pump is 20.7MPa under  $Q=1.1Q_{bep}$ . The distribution trend of equivalent stress along the blade rim is basically the same under different flow conditions. Under small flow conditions, the equivalent stress of the axial-flow pump fluctuates greatly on the SS. Because of the reduction of the relative flow angle near the LE, the flow separation on the SS is enhanced, resulting in low pressure around the LE.

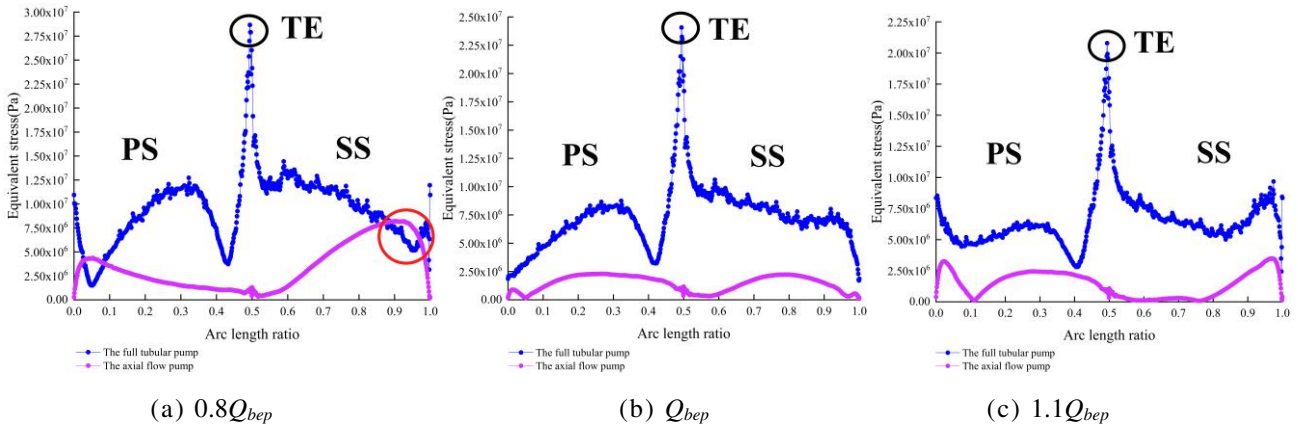


Figure. 14 The stress distribution of the blade rim

In summary, the total deformation and equivalent stress of the full tubular pump are quite different from those of the axial-flow pump. The reasons for the differences are preliminarily summarized as the following two categories. The one is clearance backflow and the other is the geometric structure. Therefore, in order to further explore the reasons for the difference, the effect of clearance backflow on its structural characteristics will be discussed in the next section as shown the Fig. 15. The structural models of unloaded rotor surface pressure(ULP) and loaded rotor surface pressure(LP) were compared to study the difference of structural performance under different flow conditions.

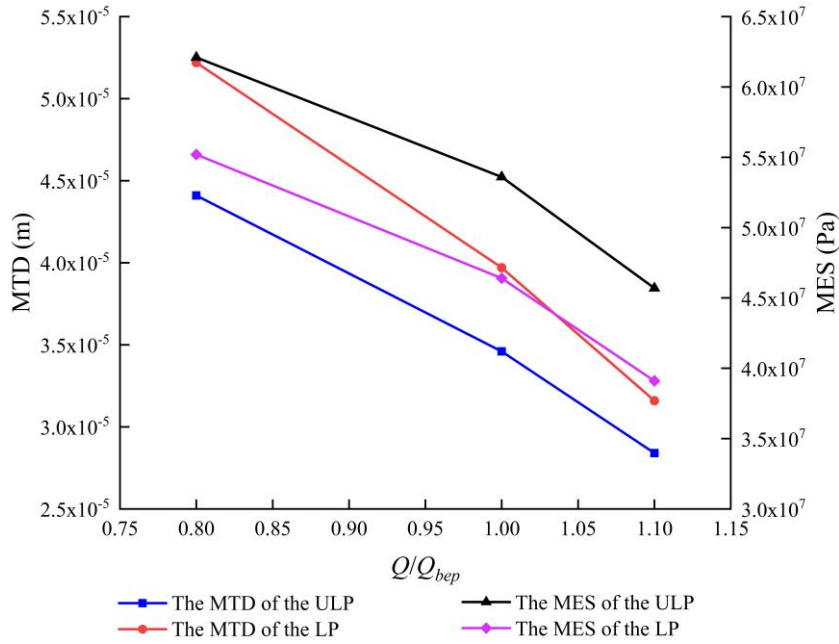


Figure. 15 Comparison of MTD and MES between ULP and LP

It can be seen from the Fig. 15 that the clearance backflow has a greater impact on the structural performance of the full tubular pump under different flow conditions. On the one hand, the clearance backflow causes the increase in the deformation. Especially under small flow conditions, the MTD of the LP increases by 20% compared to that of the ULP. On the other hand, the MES of the LP caused by the clearance backflow are smaller than that of the ULP. Compared with ULP under various flow conditions, the MTD of LP has increased by about 16%.

Compared with the axial-flow pump, it is found that the shape of the geometric structure has a greater impact on the structural performance of the tubular pump. The MTD of the ULP is much smaller than that of the axial-flow pump, accounting for 42.1%, 61.6% and 74.4% of the axial-flow pump under different flow conditions. The MES of the ULP is much higher than that of the axial-flow pump, which is 1.9 times, 2.25 times and 2.47 times that of the axial-flow pump under different flow conditions.

Based on the above analysis, it can be seen that the clearance backflow and geometric structure have a greater impact on the structural performance of the full tubular pump.

### 3.4 Modal analysis

The modal analysis in this study is based on the unidirectional FSI method. The Block Lancos method is used to perform modal analysis on the impeller under pre-stress. The pre-stress of the impeller includes the impeller's own gravity, rotation speed and the water pressure of wall surfaces acting on the impeller. The modal analysis flowchart is shown in Fig. 16.

The mode is the natural vibration characteristic of the structural system, and each mode has a specific natural frequency and vibration shape [24-26]. The impeller is the main excitation source of hydraulic excitation. The impeller rotation speed  $n$  is 950r/min, and the BPF(blade passing frequency) is 63.3Hz. If the hydraulic excitation frequency is close to the BPF and its frequency multiplier, the impeller will resonate. This article will analyze the pre-stress modal analysis of the full tubular pump and the axial-flow pump in the air medium. The first 6 natural frequencies of the impeller and the corresponding vibration mode of each order will be analyzed.

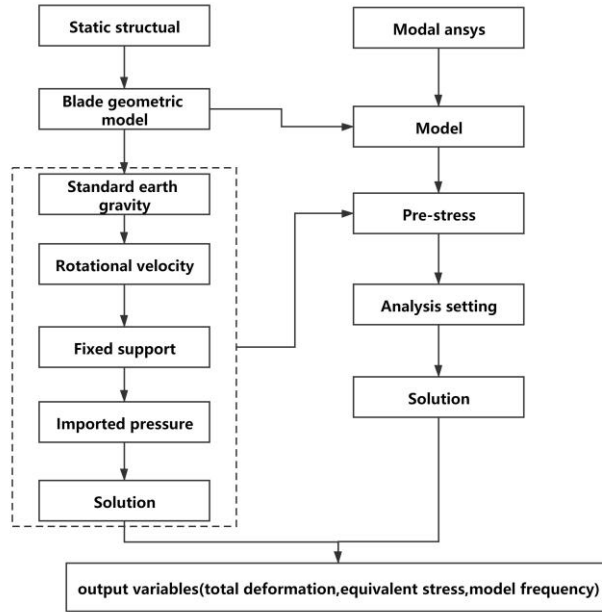


Figure. 16 The flowchart of the modal analysis

Table. 3 shows the natural frequency of the tubular pump and the axial-flow pump in each mode. The natural frequency of the full tubular pump in each mode is lower than that of the axial-flow pump affected by the rotor on the blade rim. The first-order vibration frequency of the full tubular pump is 279.9 Hz, which is 4.4 times the blade passing frequency, while the first-order vibration frequency of the axial-flow pump reaches 868.7 Hz, which is 13.7 times the blade passing frequency.

Table. 3 Modal natural frequency

Mode	First-order frequency/Hz	Second-order frequency/Hz	Third-order frequency/Hz	Fourth-order frequency/Hz	Fifth-order frequency/Hz	Sixth-order frequency/Hz
Full tubular pump	279.9	580.6	580.7	881.1	884.4	984.4
Axial-flow pump	868.7	869.8	869.8	870.1	1655.8	1655.9

Table. 4 lists the modal participation factors of the main deformation directions in each mode. The modal participation coefficient is based on the assumed unit displacement of each translational and rotational direction in the cartesian coordinate system to solve the motion mass in each direction. The larger the absolute value is, it indicates the main mode of vibration in that direction. The red dotted line in the table represents the participation coefficient with the largest absolute value of each party.

The formula of the modal participation factor is as follows.

$$\{\phi_i\}^T [M] \{\phi_i\} = 1, \quad (5)$$

$$\gamma_i = \{\phi_i\}^T \{F\}, \quad (6)$$

Where  $\gamma_i$  is the participation factor for the  $i^{\text{th}}$  mode,  $\phi_i$  is the eigenvector representing the mode shape of the  $i^{\text{th}}$  natural frequency, and  $F$  is the input force vector.

Table. 4 Modal participation factor

Mode	Frequency/Hz	Participation factor					
		X	Y	Z	ROT.X	ROT.Y	ROT.Z
1	279.9	0.18E-04	0.92E-04	3.0	-0.15E-4	0.23E-4	-0.47
2	580.6	-0.058	0.39	-0.14E-03	-0.34	0.38	0.39E-4
3	580.7	-0.39	-0.058	0.25E-04	-0.38	-0.34	-0.16E-4
4	881.1	0.23E-03	0.41E-03	-0.28E-02	0.35E-4	-0.63E-4	-0.54E-3
5	884.4	0.42E-04	0.72E-04	-2.47	-0.19E-5	0.17E-4	-0.55
6	984.4	0.20E-03	0.18E-03	0.16E-03	0.23E-4	-0.29E-4	0.25E-4

297

298

299

300

301

302

303

304

305

306

307

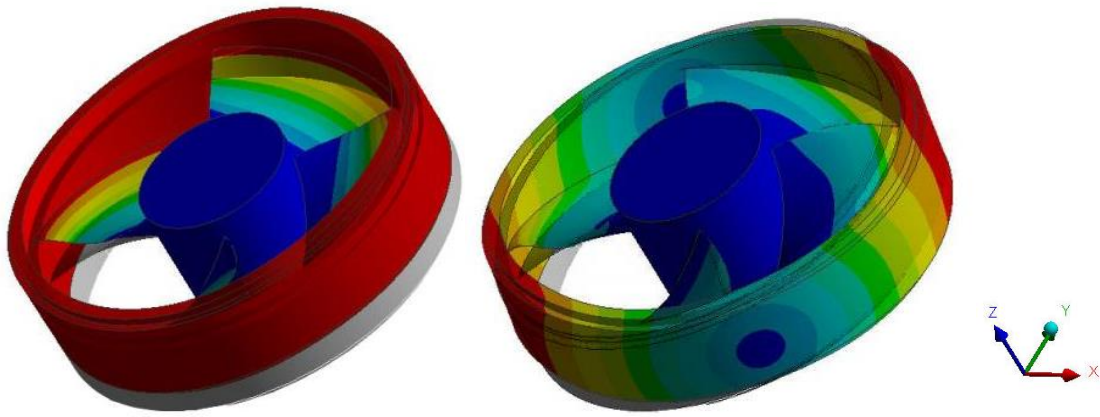
308

309

310

311

Fig. 17 shows the vibration shape of the full tubular pump in each mode. The vibration shape can be divided into deformation along the x-axis, y-axis, z-axis and torsional direction according to the cartesian coordinate system. It can be seen from the vibration shape diagram that the vibration form of the impeller can be divided into bending vibration, torsional vibration and compound vibration. The vibration mode shapes of each order modal are compared combining the participation factors of each mode in Table.4 and Fig.17. The absolute value of the participation factor of the first-order modal in the Z-axis direction is the largest, which is represented by the up and down swing along the Z-axis direction, as shown in Fig. 17(a). The absolute value of the participation factor of the second-order modal in the Y-axis direction and the torsional direction along the Y-axis is larger, and the torsional deformation of the second-order mode along the Y-axis can be clearly seen from the vibration shape of the Fig. 17(b). The vibration mode shape of 3rd modal impeller is torsional deformation along X axis. The vibration shapes of the fourth-order and sixth-order modals present the “U” type bending deformation along the Z axis, which show the vibration shape of extrusion to the middle, without showing obvious vibration mode characteristics. The fifth-order mode deforms along the torsional direction of Z axis, which is reflected that the absolute value of ROTZ direction is the largest in Table.4. Therefore, the modal participation factor has certain reference significance for the analysis of vibration modes.

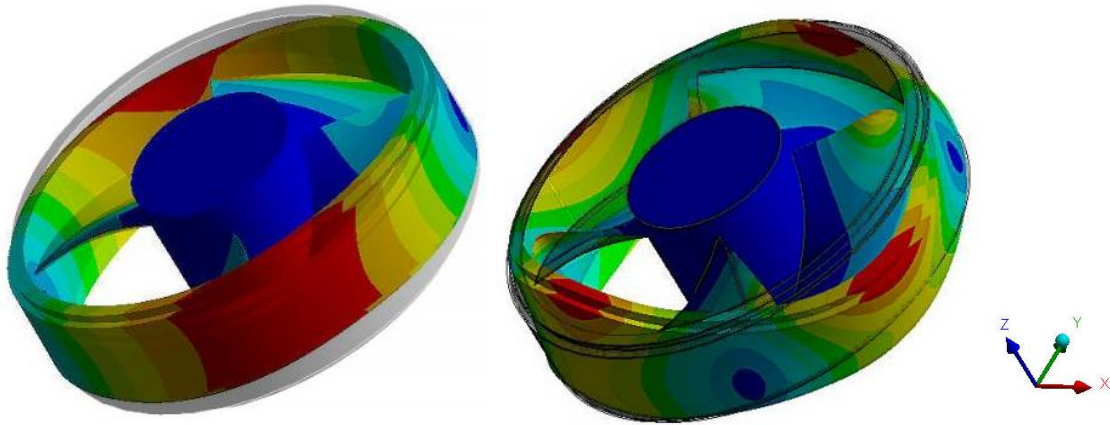


312

313

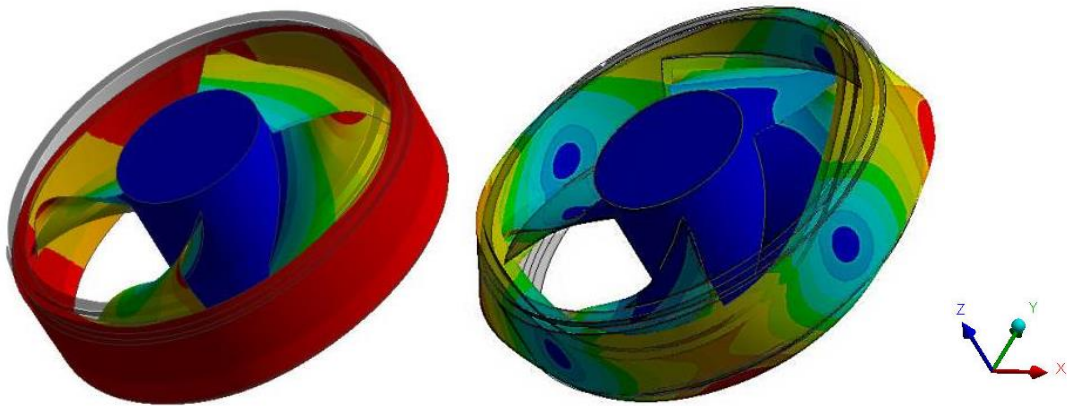
(a)First-order mode

(b)Second-order mode



(c)Third-order mode

(d)Fourth-order mode



(e)Fifth-order mode

(f)Sixth-order mode

Figure. 17 Vibration mode shape in each order modal of the full tubular pump

#### 4 Conclusions

In this paper, the FSI method is used to compare the structural strength and modal characteristics of the blades between the full tubular and the axial-flow pumps. The main conclusions are summarized as follows.

1. The distribution trend of the blade deformation and equivalent stress of the full tubular pump is basically the same under various flow conditions, but its value gradually decreases with the increase of the flow. The deformation of the blades shows a trend of gradually increasing from the hub to the rim, and the deformation is larger at the outlet of the rim, while the maximum deformation of the axial-flow pump is at the inlet of the blade. The max deformation of the full tubular pump is less than that of the axial-flow pump.
2. The equivalent stress of the full tubular pump shows a trend of first decreasing and then increasing from the hub to the rim. There are two stress concentration areas mainly distributed in the outlet of the blade rim and the area of the hub. While the equivalent stress of the axial-flow pump is reduced from the hub to the rim, and there is only one stress concentration area distributed in the center of the hub. The max equivalent stress of the axial-flow pump is smaller than that of the full tubular pump under different flow conditions.
3. The MES and MTD of the full tubular pump are located at the junction of the blade rim and the rotor. Clearance backflow and geometric shape are the main reasons for the difference in structural performance between the tubular flow pump and the axial-flow pump. It is very necessary to pay attention to the rigidity of the full tubular pump rim.
4. The natural frequency of each order modal for the full tubular pump is less than that of the axial-flow pump. The natural frequency of first-order mode for the full tubular pump is 279.9Hz, and the modal participation factor in Z-axis is 3.0, which the absolute value is max in the Z-axis direction and represents by the up and down swing along the Z-axis

338 direction. The modal participation factor has certain reference significance for analyzing the vibration mode shape.

### 339 **Data Availability**

340 All the data in this paper are obtained by physical experiment and numerical simulation respectively, and the data used to  
341 support the findings of this study are available from the corresponding author upon request.

### 342 **Acknowledgments**

343 Data curation, Lijian Shi, Li Wang, Shiji Chu; Formal analysis, Fangping Tang; Writing–original draft, Jun Zhu;  
344 Writing–review & editing, Yuhang Jiang, Jie Yu, Tian Xu.

### 345 **Funding**

346 This work was supported by the National Natural Science Foundation of China (grant number 51376155); the Natural  
347 Science Foundation of Jiangsu Province of China (grant number BK20190914); China Postdoctoral Science Foundation  
348 Project (2019M661946); the Natural Science Foundation of Jiangsu Higher Education Institutions of China (grant  
349 number 19KJB570002); the National Science Foundation of Yangzhou of China (grant number YZ2018103); the Priority  
350 Academic Program Development of Jiangsu Higher Education Institutions (grant number PAPD).

### 351 **Conflicts of Interest:**

352 The authors declare no conflict of interest.

### 353 **Nomenclature:**

354	$D$	impeller diameter, mm.
355	$Q$	flow, L/s
356	$\rho$	the density, kg/m <sup>3</sup> .
357	$g$	local acceleration of gravity, m/s <sup>2</sup> .
358	$H$	head, m.
359	$\eta$	efficiency, %.
360	$n$	rotation speed, r/min.
361	$bep$	best efficiency point.
362	$\mu_t$	the turbulence viscosity.
363	$C_\mu$	the empirical constant according to the recommended value of Launder.
364	$G_k, G_b$	the generation term of turbulent kinetic energy $k$ .
365	$Y_M$	the contribution of pulsation expansion.
366	$C_{1\varepsilon}, C_{2\varepsilon}, C_{3\varepsilon}$	empirical constants according to the recommended value of Launder.
367	$\sigma_k, \sigma_\varepsilon$	the Prandtl Numbers corresponding to turbulent kinetic energy $k$ .
368	$\sigma_\varepsilon$	the Prandtl Numbers corresponding to dissipation rate $\varepsilon$ .
369	$S_k, S_\varepsilon$	user-defined source terms.
370	$u_i$	the fluid velocity component in the direction of the coordinate $x_i$ , m <sup>2</sup> /s.
371	$S$	a generalized source term.
372	FSI	fluid-structure interaction.
373	MTD	the maximum total deformation, m.
374	MES	the maximum equivalent stress, Pa
375	PS	the pressure surface of blade.
376	SS	the suction surface of blade.
377	TE	the trailing edge of blade.
378	LE	the leading edge of blade.
379	ULP	the unloaded rotor surface pressure.
380	LP	the loaded rotor surface pressure.
381	BPF	the blade passing frequency, Hz.
382	$\gamma_i$	the participation factor for the $i^{\text{th}}$ mode.
383	$\phi_i$	eigenvector representing the mode shape of the $i^{\text{th}}$ natural frequency.
384	$F$	Input force vector.
385	[M]	the structural mass matrix.
386	[C]	the structural damping matrix.
387	[K]	the structural stiffness matrix.
388	$(\dot{x})$	the structural velocity.
389	$(x)$	the structural displacement.
390	$(\ddot{x})$	the structural acceleration.

391	{F}	the flow field force of the structure under the FSI
392	$E$	Young modulus, MPa.
393	$\mu$	Poisson ratio
394	$\sigma_s$	Yield strength, MPa.

## 395 References

- 396 1. Liu, C., 2015. Researches and Developments of Axial-flow Pump System. Transactions of the Chinese Society for  
397 Agricultural Machinery. 46(6), 49–59.
- 398 2. Shi, L.J., Jiao, H.F., Gou, J.L., Yuan, Y., Tang, F.P., Yang, F., 2020. Influence of backflow gap size on hydraulic  
399 performance of full-flow pump. Transactions of the Chinese Society for Agricultural Machinery. 51(04), 139-146.
- 400 3. Shi, L.J., Yuan, Y., Jiao, H.F., Tang, F.P., Cheng, L., Yang, F., Jin, Y., Zhu, J., 2021. Numerical investigation and  
401 experiment on pressure pulsation characteristics in a full tubular pump. Renewable Energy. 163, 987-1000.
- 402 4. Shi, L.J., Zhang, W.P., Jiao, H.F., Tang, F.P., Wang, L., Sun, D.D., Shi, w., 2020. Numerical simulation and  
403 experimental study on the comparison of the hydraulic characteristics of an axial-flow pump and a full tubular pump.  
404 Renewable Energy, 153:1455-1464.
- 405 5. Chirag, T., Michel J, C., 2017. Fluid-structure interactions in Francis turbines: A perspective review. Renewable and  
406 Sustainable Energy Reviews. 68(Part 1):87-101.
- 407 6. Dorji, U., Ghomashchi, R., 2014. Hydro turbine failure mechanisms: an overview. Eng Fail Anal. 44, 136–47.
- 408 7. Zhou, L.J., Wang, Z.W., Xiao R.F., Luo, Y.Y., 2007. Analysis of dynamic stresses in Kaplan turbine blades.  
409 Engineering Computations. 24(7-8), 753–62.
- 410 8. Wu, G.K., Luo, X.Q., Feng, J.J., Li, W.F., 2015. Cracking reason for Francis turbine blades based on transient fluid  
411 structure interaction. Transactions of the Chinese Society for Agricultural Machinery. 31(8), 92–98.
- 412 9. Kan, K., Zheng, Y., Fu, S.F., Yang, C.X., Zhang, X., 2017. Dynamic stress of impeller blade of shaft extension tubular  
413 pump device based on bidirectional fluid-structure interaction. Journal of Mechanical Science & Technology. 31(4),  
414 1561-1568.
- 415 10. Kan, K., Zheng, Y., Chen, H.X., 2019. Study into the Improvement of Dynamic Stress Characteristics and Prototype  
416 Test of an Impeller Blade of an Axial-Flow Pump Based on Bidirectional Fluid–Structure Interaction. Applied  
417 Sciences. 9(17), 3601.
- 418 11. Schneider, A., Will, B., Böhle, M., 2013. Numerical Evaluation of Deformation and Stress in Impellers of Multistage  
419 Pumps by Means of Fluid Structure Interaction. In: ASME Fluids Engineering Division Summer Meeting.
- 420 12. Pei, J., Meng, F., Li, Y.J., Yuan, S.Q., Chen, J., 2016. Fluid–structure coupling analysis of deformation and stress in  
421 impeller of an axial-flow pump with two-way passage. Advances in Mechanical Engineering. 8(4).
- 422 13. Zhang, L.J., Wang, S., Yin, G.J., Guan, C.N., 2019. Fluid–structure interaction analysis of fluid pressure pulsation and  
423 structural vibration features in a vertical axial pump. Advances in Mechanical Engineering. 11(3):1.
- 424 14. Li, W. Yang, Y.F., Shi, W.D., Ji, L.L., Jiang, X.P., 2015. Mechanical Properties of Mixed-flow Pump Impeller Based  
425 on Bidirectional Fluid-structure Interaction. Transactions of the Chinese Society for Agricultural Machinery. 46(12),  
426 82-88.
- 427 15. Li, W., Ji, L.L., Shi, W.D., Jiang, X.P., Zhang, Y., 2016. Vibration characteristics of the impeller at multi-conditions in  
428 mixed-flow pump under the action of fluid-structure interaction[J]. Journal of Vibroengineering. 18(5), 3213-3224.
- 429 16. Li, C.Y., Zheng, Y., Zhang, Y.Q., Kan, K., Xue, X.Y., Rodriguez, E.F., 2020. Stability Optimization and Analysis of a  
430 Bi-Directional Shaft Extension Pump[J]. Journal of Fluids Engineering. 142(7), 071203.
- 431 17. Deng, Z.P., Hu, Q.H., Dong, Y.F., Li, Y., 2016et al. Comparison between one-way and two-way fluid-structure  
432 interaction simulations of a horizontal tidal current turbine. In: The second conference of global Chinese scholars  
433 hydrodynamics.
- 434 18. Benra, F.K., Dohmen, H.J., Pei, J., Schuster, S., Wan, B., 2011. A Comparison of One-Way and Two-Way Coupling  
435 Methods for Numerical Analysis of Fluid-Structure Interactions. Journal of Applied Mathematics.
- 436 19. Zhu, R, Chen, D.D., Wu, S.W., 2019. Unsteady Flow and Vibration Analysis of the Horizontal-Axis Wind Turbine  
437 Blade under the Fluid-Structure Interaction[J]. Shock and Vibration. 2019, 1-12.
- 438 20. Javanmardi, N., Ghadimi, P., 2019. Hydroelastic analysis of surface-piercing propeller through one-way and two-way  
439 coupling approaches[J]. Proceedings of the Institution of Mechanical Engineers Part M Journal of Engineering for the  
440 Maritime Environment. 233(5), 844-856.
- 441 21. Wijesooriya, K., Mohotti, D., Amin, A., Chauhan, K., 2021. Comparison between an uncoupled one-way and two-way  
442 fluid structure interaction simulation on a super-tall slender structure[J]. Engineering Structures. 229, 111636.

- 443 22. Shi L.J, Zhu J, Yuan, Y, Tang, F.P., Huang, P.L., Zhang, W.P., Liu, H.Y., Zhang, X.W., 2021. Numerical Simulation  
444 and Experiment of the Effects of Blade Angle Deviation on the Hydraulic Characteristics and Pressure Pulsation of an  
445 Axial-Flow Pump. *Shock and Vibration*. 2021, 1-14.
- 446 23. Shi, L.J., Zhu, J, Tang, F.P., Wang, C., 2020. Multi-Disciplinary Optimization Design of Axial-Flow Pump Impellers  
447 Based on the Approximation Model. *Energies*. 13(4), 1-19.
- 448 24. Kang C, Zhu Y, Li Q. Effects of hydraulic loads and structure on operational stability of the rotor of a molten-salt  
449 pump[J]. *Engineering Failure Analysis*, 2020, 117:104821.
- 450 25. Peng, G.J., Zhang Z.R., Bai, L., 2021. Wet Modal Analyses of Various Length Coaxial Sump Pump Rotors with  
451 Acoustic-Solid Coupling. *Shock and Vibration*. 2021(3), 1-9.
- 452 26. Qi, Y., 2015. Stress and Modal Analysis of Bi-Directional Pump Blades. Yangzhou University, Yangzhou, Jiangsu,  
453 China.